

Case History

The relation between stimulated shear fractures and production in the Barnett Shale: Implications for unconventional oil and gas reservoirs

Alex Hakso¹ and Mark Zoback¹

ABSTRACT

Economic production from extremely low permeability unconventional reservoirs is accomplished through multistage slick water hydraulic fracturing, which generates opening-mode hydraulic fractures and induces shear slip on preexisting fractures in the surrounding formation. We have addressed the critical contribution of the stimulated shear fracture network on production. We found production decline curves from tens of thousands of wells in four unconventional plays in the U.S. (two oil and two gas). These data indicate that during the early years of production: (1) Production is dominated by linear flow from the extremely low permeability matrix into much more permeable

fracture planes, (2) the rapid decrease in production rates is a natural consequence of pressure depletion in the matrix within several meters of the more permeable planes, and (3) the cumulative area of permeable fracture planes created during stimulation is an important factor affecting cumulative production. Using data from two case studies in the Barnett Shale, we estimate the area of the fracture network from the microseismicity generated during hydraulic fracturing operations. The data from one study demonstrates that the cumulative area of the shear fracture network is needed to match production data. With data from the other case study, we demonstrate that the relative fracture area created during each stage correlates well with the relative stage-by-stage production determined from distributed temperature sensing.

INTRODUCTION

Multistage hydraulic fracturing enhances production from unconventional oil and gas reservoirs by inducing both opening mode hydraulic fractures that propagate in a direction perpendicular to the minimum horizontal principal stress and shear slip on preexisting fractures and faults in the volume of rock surrounding the hydraulic fractures. This shear slip manifests itself as a “cloud” of microseismic events surrounding the hydraulic fractures (see Maxwell and Cipolla, 2011). Shear slip can be triggered on these preexisting fractures and faults because low-viscosity *slick water* (a typical fracturing fluid) allows the pressure in the hydraulic fractures to leak out and increase the pore pressure in the fractures of surrounding rock mass. Typical matrix permeabilities of major unconventional range from tens to a couple of hundred nanodarcies (Luffel et al., 1993; Kang et al., 2011; Heller et al., 2014; Bhandari

et al., 2015; Al-Ismail and Zoback, 2016). Whereas multistage hydraulic fracturing likely has little effect on matrix permeability, the induced shear deformation on the naturally rugose preexisting fracture planes increases permeability through dilatancy. Laboratory studies show that this occurs even with slip magnitudes of less than 0.1 mm (Ye et al., 2017), the approximate amount of slip expected of typical magnitude -2 microseismic events (Zoback and Kohli, 2019). Several authors have argued that the “robustness” of the microseismic cloud accompanying multistage hydraulic fracturing is correlative with production. Although this is logical, quantitative predictions using parameters such as the number of microseismic events, the event density, or the stimulated rock volume have proven to be difficult to use quantitatively (Cipolla and Wallace, 2014).

In the first section of this paper, we examine the rate at which production decreases for thousands of unconventional oil wells in the

Manuscript received by the Editor 20 July 2018; revised manuscript received 20 June 2019; published ahead of production 4 September 2019; published online 30 October 2019.

¹Stanford University, School of Earth Sciences, Department of Geophysics, Stanford, California, USA. E-mail: ahakso@alumni.stanford.edu; zoback@stanford.edu.

© 2019 Society of Exploration Geophysicists. All rights reserved.

Eagle Ford and Bakken Formations and thousands of gas wells in the Barnett and Marcellus Formations. In each case, we show that the rate at which the production rate declines during the first two to three years of production follows $1/\sqrt{t}$, as expected for linear flow (Arps, 1945; Joshi and Lee, 2013). Katz et al. (1959) show that linear flow into permeable fractures implies a production rate that is proportional to $A\sqrt{k_m}$, where k_m is the matrix permeability. In the context of slick water hydraulic fracturing in unconventional reservoirs, A represents the total surface area — the hydraulic fractures and shear fractures in contact with the extremely low permeability matrix.

In the second section of the paper, we analyze the microseismic events associated with shear fracture networks created during multi-stage hydraulic fracturing in two case studies from the Barnett Shale. In one case, we carried out a geomechanical analysis to show that the orientation of fault planes in the shear fracture network determined from earthquake focal plane mechanisms agrees quite well with those predicted to slip based on analysis of an image log in the stimulated well. In the final section of the paper, we consider production from the two data sets to support the concept that the contact area of the shear fracture network is critically important. In other words, in the context of the $A\sqrt{k_m}$ model of Katz et al. (1959), production from extremely low unconventional formations with

matrix permeabilities in the order of 100 nD can only be explained if we consider the surface areas represented by the permeable hydraulic fractures and the permeable shear fracture network.

THE RAPID DECLINE OF PRODUCTION RATES AND LINEAR FLOW

Figure 1 shows average decline curves for thousands of unconventional oil (Eagle Ford, Bakken) and gas (Barnett, Marcellus) wells. The mean monthly production data are shown for wells in two-year cohorts from the first years of appreciable production, where a cohort is comprised of wells that began producing in the same time window. To obtain robust averages, any well that did not produce for at least 24 months was excluded, as were two-year cohorts with less than 350 wells. After applying these criteria, a total of 45,440 wells remain, representing more than 7500 wells in each reservoir.

Whereas individual wells show complex behavior due to operational issues (such as interventions targeted at improving production), averaging so many wells provides reasonably clean decline curves. As is well known, monthly production rates decrease rapidly during the first two to three years of production (Figure 1a). The center column in Figure 1 shows average cumulative production per well

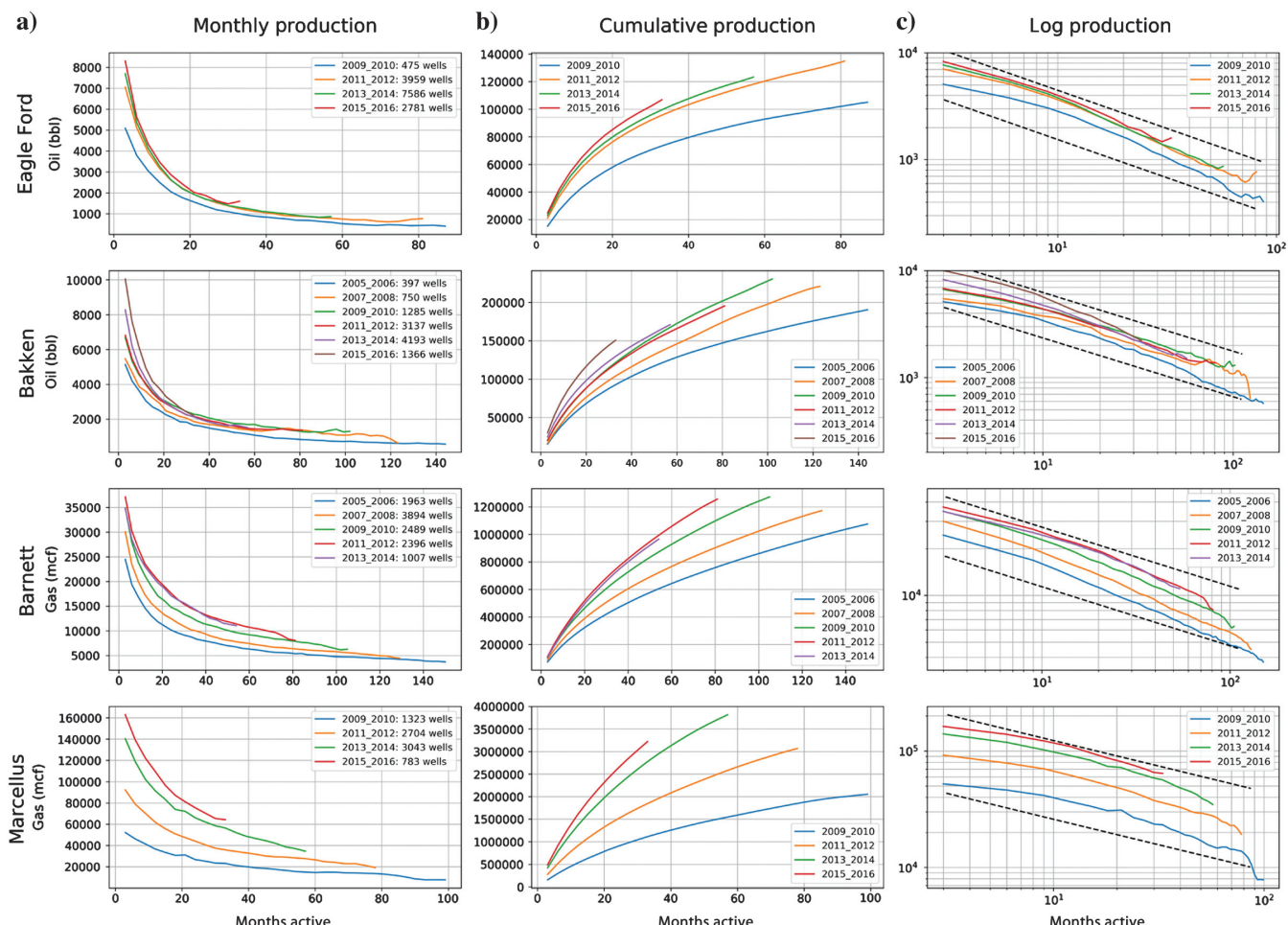


Figure 1. Production is grouped and averaged by reservoir in two-year increments. Panel (a) shows monthly production rates (averaged over quarters), (b) shows cumulative production, and (c) shows monthly production rates in log-log space to demonstrate that production rates decline with a rate similar to $1/\sqrt{t}$ (as indicated by the dashed lines).

as a function of time. In each reservoir, improved production practices (such as longer horizontal wells and more and larger hydraulic fracturing stages) result in production rates that increase monotonically from each two-year cohort to the next. This is most dramatic in the Barnett, where the technologies used for horizontal drilling and multistage hydraulic fracturing were rapidly evolving, and in the Marcellus, where significant improvements in completion methodologies were developed between 2009 and 2014. Note that the most recently drilled wells in the Eagle Ford, Bakken, and Marcellus show significant production, even after three years.

As mentioned above, a $1/\sqrt{t}$ decline rate indicates linear flow from the low-permeability matrix to more permeable planes. In linear flow, production rate q is proportional to $1/\sqrt{t}$, as given by

$$q = \frac{1}{2} \frac{\alpha}{\sqrt{t}}, \quad (1)$$

where, for dry gas reservoirs,

$$\alpha = A \left(\frac{P_r^2 - P_{bhf}^2}{P_s} \right) \sqrt{\frac{c_g \phi_m k_m}{\pi \eta}}, \quad (2)$$

where P_r is the reservoir pressure, P_{bhf} is the bottom hole flowing pressure, P_s is the atmospheric pressure, c_g is the gas compressibility, ϕ_m is the matrix porosity, η is the gas viscosity, k_m is the matrix permeability, and A is the area of permeable fractures, as discussed above. As mentioned above, equations 1 and 2 are sometimes referred to as an $A\sqrt{k_m}$ model to emphasize the fact that for given formation pressure, porosity, fluid viscosity, and so on, as formation permeability decreases, the area of contact with the formation A must increase to achieve comparable production rates. For oil, c_g is replaced by a constant with units pressure⁻¹ and the driving pressure term is slightly different (Katz et al., 1959). The cumulative production is obtained by integrating equation 1

$$q = \alpha \sqrt{t}, \quad (3)$$

which is shown in the center column of Figure 1.

To emphasize the observation that production rates decline with $1/\sqrt{t}$, we replotted the data in the left column of Figure 1 in the right column in log-log space. This implies that $\log(q)$ should decline with a slope of $-1/2$ as indicated by

$$\log(q) = \log\left(\frac{1}{2}\alpha\right) - \frac{1}{2}\log(t). \quad (4)$$

During the first three years of production, the average slope of all two-year cohorts in all reservoirs shown in Figure 1 is -0.503 , with an R^2 value of 0.98, indicating linear flow during the first several years of production. With data from 66 wells in the Barnett Shale, Patzek et al. (2014, Figure 6) show that average production rates decrease with time as $1/\sqrt{t}$. Using a linear flow model considering only the matrix and permeable hydraulic fractures, they match the average production data of Barnett wells. However, we discuss below that their assumed matrix permeability of 400–500 nD is almost an order of magnitude higher than indicated by the laboratory measurements such that it is important to consider the surface area created in the stimulated fracture network (as well as that of the hydraulic fractures) to match production.

The right column of Figure 1 shows that as production continues after three years, the rate at which production declines increases. This might reflect interaction between individual fractures, matrix permeability (or fracture conductivity) decreasing with depletion, or a slow transition to radial flow, which would imply a decay proportional to $1/t$. Long-term decreases in production rates are discussed in more detail by Joshi and Lee (2013).

MICROSEISMICITY AND SHEAR FRACTURE NETWORKS

In this section, we analyze two microseismic data sets gathered during hydraulic fracturing operations in the Barnett Shale, which will be referred to as the Barnett I and II data sets. Whereas shear slip on preexisting faults stimulated during hydraulic fracturing might slip slowly and not produce detectable microseismic events (see Maxwell et al., 2008; Zoback et al., 2012), the microseismic events can be used to provide, at the very least, a lower bound estimate of the cumulative area created in the stimulated fracture network. In addition, laboratory studies indicate that slowly moving shear fractures might not increase permeability significantly (Wu et al., 2017).

The Barnett microseismic data sets will be used to generate fracture network models based on event locations and magnitudes. Shear fracture networks are characterized by fracture intensity, orientation, size, and spatial distribution. In the sections below, we argue that these parameters impact production from unconventional reservoirs because they control the distance that hydrocarbons must flow through the matrix to reach high-permeability pathways to the hydraulic fractures, and then to the wellbore. Given the extremely low matrix permeability of unconventional reservoirs, introducing as much surface area as possible during stimulation effectively minimizes diffusion distances through the matrix, thus enhancing production through stimulation. The reported magnitudes are moment magnitudes and account for source-receiver distance, receiver frequency response, and rms noise levels. Because we will consider the attributes of the shear fracture network statistically, a high level of accuracy in individual event locations, magnitudes, and assigned stress drops is not required.

In Barnett I and II, each fracture stage was monitored by two downhole geophone arrays, where a stage refers to an isolated perforation zone that is pressurized in an injection period of several hours. Figure 2 shows plan views of the stimulated wells, the wells in which microseismic monitoring arrays were deployed, and associated microseismicity. Events are colored by stage. There were five stages in the Barnett I case study and eight stages in the Barnett II study. Microseismic event intensity varies significantly by stage, and event locations sometimes scatter across multiple stages. This can result from (1) inaccurate event locations (Hakso and Zoback, 2017), (2) microseismic events propagating along preexisting fault systems (Farghal and Zoback, 2015), or (3) poor zonal isolation (many stage 2 events occur in the vicinity of stage 1 in the Barnett II data set).

Figure 3 (modified from Zoback and Lund Snee, 2018) illustrates the manner in which elevated pore pressure during hydraulic fracturing triggers slip. Using Mohr circles and stereonets, the figure illustrates how elevated pore pressures affect induced shear slip considering the population of fractures associated with the Barnett I data set. Note that for the Mohr circles shown, the abscissa indicates total stress S_{ij} , not effective stress. Presentation in this manner

makes the intercept of the frictional faulting line correspond to the initial, unperturbed pore pressure. For the purposes of illustration, we assume near-hydrostatic pore pressure and a coefficient of friction of 0.6. We ignore cohesion, which is likely to be quite small. Although friction can vary depending on clay content, an average

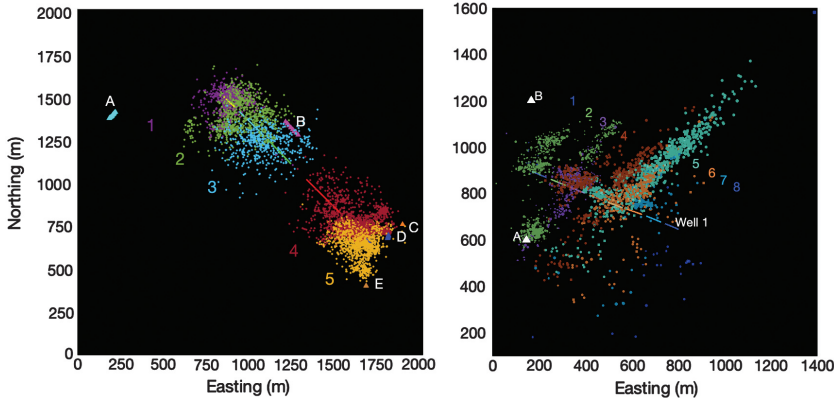


Figure 2. Plan view of two hydraulically stimulated wells in the Barnett with associated seismicity: Barnett I (left) and Barnett II (right). In the Barnett I data set, seismic monitoring arrays were deployed in two of the five wells labeled A–E, with the deployment wells moving heelward with stimulation to minimize source-receiver distance. In the Barnett II data set, monitoring of all eight stages was performed from monitoring wells A and B. The individual stages (and associated microseismicity) are indicated by numbers and colors.

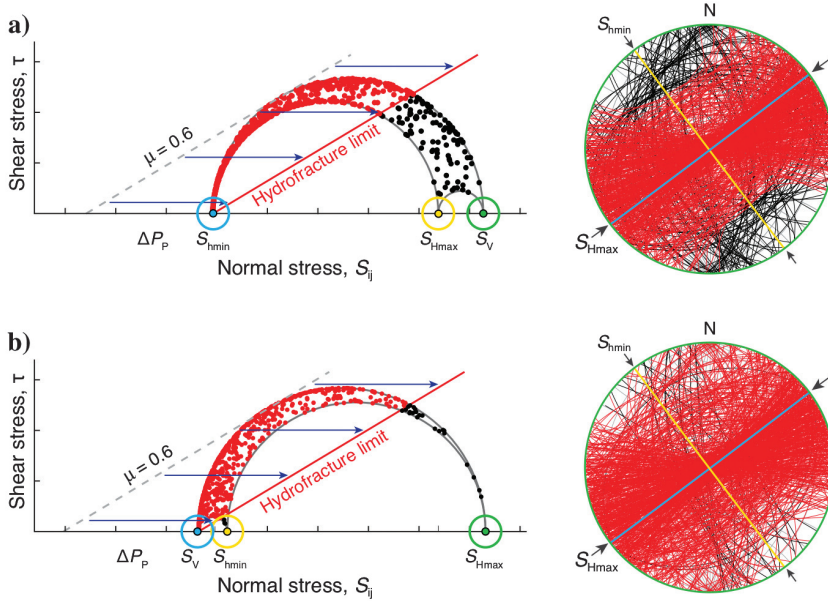


Figure 3. Mohr diagrams and stereonet images illustrating (a) the shear and normal stress on preexisting fractures observed in the wellbore image log and (b) planes obtained from focal mechanisms where the likely slip plane was identified. In (a), the fracture planes stimulated in shear at a pressure perturbation equal to the least principal stress are shown in red. The planes not stimulated are shown in black. Note the excellent comparison between the fractures expected to slip on the basis of a geomechanical analysis of the fractures observed in the image log with those that did slip as indicated by the microseismicity. The blue and yellow vertical planes shown in the stereonet (and the poles shown in the Mohr diagram) are parallel and perpendicular to the direction of hydraulic fracture propagation, respectively. The green horizontal plane (and the green pole) represents horizontal bedding planes. Modified from Zoback and Lund Snee (2018).

value of approximately 0.6 is quite reasonable for the Barnett Shale (Kohli and Zoback, 2013). The fracture planes shown in the Mohr circle and stereonet images in Figure 3a were obtained from an image log in the horizontal well. The planes in Figure 3b represent slip planes determined from a geomechanical analysis of focal plane mechanisms (Kuang et al., 2017). The blue and yellow planes shown in the stereonet are hypothetical planes normal to $S_{h\min}$ (subparallel to hydraulic fractures) and normal to $S_{h\max}$, respectively. We show these planes because it is sometimes assumed that preexisting fractures in unconventional reservoirs are aligned parallel and perpendicular to the current principal stresses. It is clear that this is not the case. We also show in green a hypothetical plane normal to S_V (simulating horizontal bedding planes) as it is sometimes argued that bedding plane slip can be significant during hydraulic fracturing.

The stress state was determined using established wellbore methods and focal mechanism inversions (see Kuang et al., 2017). The stress state is well-constrained to be a normal/strike-slip faulting stress state. The vertical principal stress S_V is maximum with the maximum horizontal principal stress ($S_{h\max}$) being only slightly less. Whereas there may be significant stress changes near the tip of a propagating hydraulic fracture (or immediately adjacent to a well that is being stimulated), there are no significant stress changes expected in the volume of rock associated with the shear fracture network. Kuang et al. (2017) carry out separate stress inversions for four stages in the Barnett 1 data set and obtain identical stress states (see Figure 7.11 in Zoback and Kohli, 2019). In addition, lineations of microseismic events associated with hydraulic fracturing (those caused by the process of pressure leak-off from hydraulic fracture planes) are consistent from stage to stage, indicating no significant stress reorientation from stage to stage (see Figure 7.12 in Zoback and Kohli, 2019).

The planes in Figure 3a shown in red are those expected to be stimulated during hydraulic fracturing by a pressure equal to the least principal stress. In other words, in the absence of stimulation, essentially all of the planes would be considered geologically inactive fractures and faults, frequently mineralized with calcite (Gale et al., 2014). The planes shown in Figure 3b represent planes that did slip as determined from the focal plane mechanisms of the microseismic events (Kuang et al., 2017). For comparison, the total number of planes shown was scaled to show a comparable number to that shown in the upper part of the figure because focal plane mechanisms could be computed only for the 113 largest events. The excellent comparison between these figures indicates that orientation of the slipping fractures and faults in the stimulated shear fracture network

have the same overall orientation as those expected to slip from the geomechanical analysis of the planes observed in the image log. In addition, the fact that these planes slipped in shear during stimulation means that the pressure resulting from hydraulic fracturing operations reached each of these fault planes to initiate slip. Thus, there is an interconnected, permeable fracture network in contact with the relatively impermeable shale matrix in the volume of rock surrounding the hydraulic fractures.

The area S associated with each event is calculated through the seismic moment M_o and stress drop $\Delta\tau$. For a circular fault, the area is given (Stein and Wysession, 2003) as

$$S = \pi \left(\frac{7M_o}{16\Delta\tau} \right)^{\frac{2}{3}}. \quad (5)$$

Rectangular faults have a slightly different shape parameter (the ratio of length to width, rather than π), but the following analysis is essentially unaffected by the assumption of the shape of the fracture. Calculating stress drops for microseismic data is not possible due to the limited bandwidth of the recorded seismograms. Because of the extremely small size of microseismic events, data to several thousand Hz would be needed. From other studies, we know that stress drop distributions are scale-invariant and generally follow a log-normal distribution (Imanishi and Ellsworth, 2006; Allmann and Shearer, 2009). Several studies (e.g., Goertz-Allmann et al., 2011; Clerc et al., 2016; Cocco et al., 2016; Huang et al., 2016) have examined stress drops over an extremely wide range of earthquake sizes. Each study finds values in the range from 10^{-1} to 10^2 MPa, with median stress drops of less than 10 MPa, and no discernible trend with earthquake size. The complete stress drop for a given geomechanical context provides an upper bound (the maximum available shear stress in the studies reported here is approximately 8.5 MPa). In this study, a log-normal stress drop distribution is constructed such that few events exceed complete stress drop, and the standard deviation is representative of empirical studies of average stress drops found in the literature. Hence, the distribution is centered on a stress drop of 0.5 MPa. Note that the radius of a circular fault as given in equation 5 is proportional to the cube root of the stress drop, mitigating the impact of any difference between assumed and actual stress drop distributions.

To visualize the fracture networks implied by the microseismicity associated with the Barnett I data set, Figure 4 shows a $100 \times 100 \times 100$ m visualization in the area of the densest concentration of seismicity in the vicinity of stage 4. The colors represent groups of nearby intersecting fault planes. The locations are those reported by the microseismic contractor, plane sizes are given determined from equation 5, and plane orientations are determined from the focal mechanisms in the context of the local stress field. Note that there is a wide distribution of shear fractures and fracture orientations in the area between the hydraulic fractures, implying a well-connected network of shear fractures in contact with the low-permeability matrix. Whereas it is not realistic to consider this image an accurate representation of the fracture network given the large relative location uncertainties in this data set (Hakso and Zoback, 2017), the total production is controlled by the total area of permeable fractures in contact with the reservoir (equations 1 and 2); the fracture networks modeled in this study should be viewed as statistically representative, rather than as precise models.

The magnitude distribution for the events in the Barnett II data set is shown in Figure 5a. Note the very high b slope, a characteristic of microseismic data sets (e.g., Maxwell, 2014; Eaton and Maghsoudi, 2015). Randomly drawing from the empirical stress drop distribution yields a median source radius of approximately 1 m as most events are approximately of magnitude -2 (Figure 5b). Figure 5c shows plan views of fracture networks generated from stress drop distributions with median stress drops of 0.5 and 0.1 MPa to illustrate the impact of a fivefold change in the median stress drop. Again, the colors represent groups of nearby intersecting fault planes. To calculate total surface area from the microseismicity created in every stage, we extrapolated the total number of events down to magnitude -2.25. Although many more smaller events might have occurred but were undetected, we did not extrapolate the number of events further because smaller magnitudes are associated with extremely small amounts of surface area. As mentioned above, because aseismic slip may be occurring during stimulation, the cumulative area calculated from the microseismic events represents a conservative estimate of the created surface area.

IMPLICATIONS FOR PRODUCTION

It is well-known that many factors affect successful multistage hydraulic fracturing stimulation in extremely low-permeability unconventional formation. These include stage design (stage length, the number of perforation clusters, perforation diameter, etc.), the

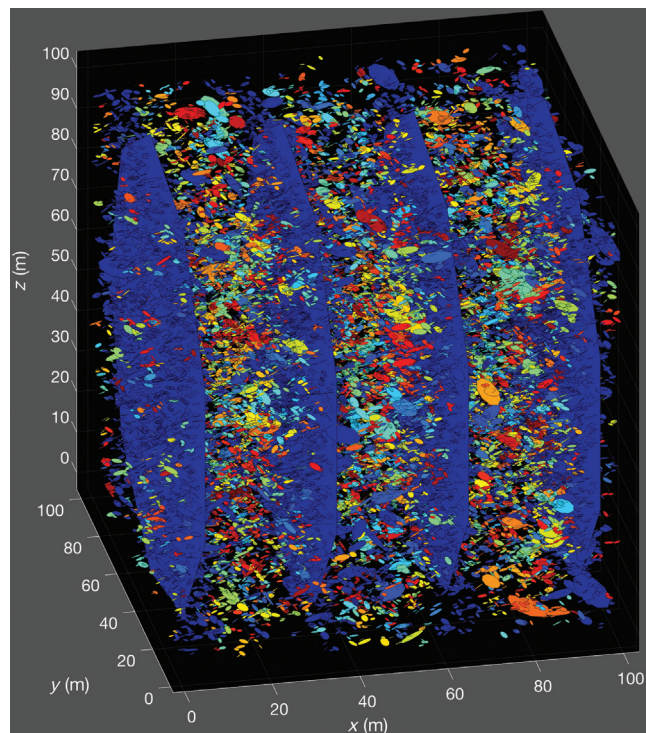


Figure 4. The four large, parallel planes represent hydraulic fractures extending from the stage. Each other plane represents a fault plane implied by microseismicity in the vicinity of stage 4 of the Barnett I data set. The colors represent groups of intersecting fault planes in this model. As slip was stimulated on all the fault planes during hydraulic fracturing, the entire network of fault planes shown is connected to the pressure leaking off from one or my hydraulic fractures.

hydraulic fracturing fluid (fluid viscosity and additives, the type and amount of proppant, etc.) and the pumping program (pumping rates, cumulative volumes, and specification of what gets pumped when). In this section, we only consider the correlation between production in the Barnett Shale wells and the area represented by the shear fracture network.

As mentioned above, Patzek et al. (2014) successfully model production from average Barnett wells assuming linear flow into 10 hydraulic fractures with a cumulative propped surface area of 140,000 m² and an average matrix permeability of 400–500 nD.

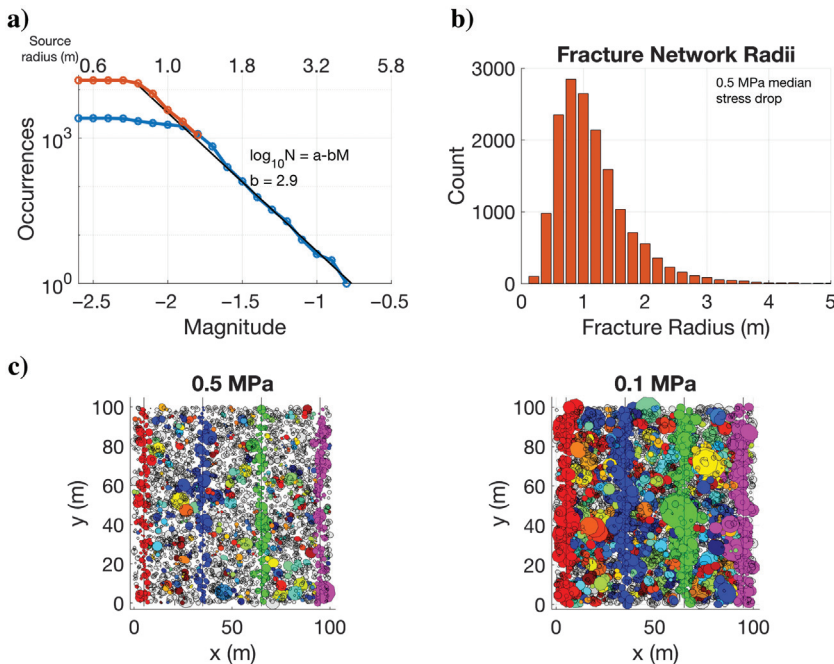


Figure 5. (a) The earthquake catalog is complete to approximately -1.9, (observed events in blue), here extrapolated to -2.25 (red). Source radius is shown on the top x-axis, calculated for a stress drop of 0.5 MPa. (b) This results in a distribution of fracture radii with a median fracture radius of 1.08 meters, with a long tail to the right. (c) Assuming a 5x smaller stress drop in a representative region of dense seismicity results in a fracture network with 40% smaller fracture radii, but otherwise identical characteristics. The colors represent groups of nearby intersecting fault planes.

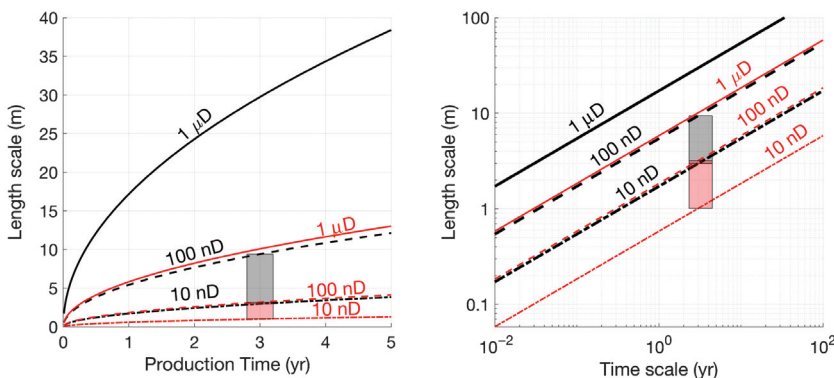


Figure 6. The time required for methane to diffuse through typical matrix permeabilities is given on a linear scale on the left and log-log scale on the right. The corresponding time/distance relationship for oil is shown in red. The gray and pink boxes reflect a representative range of matrix permeabilities for unconventional reservoirs.

Laboratory measurements typically indicate the matrix permeability of Barnett samples of 100 nD or less (Kang et al., 2011; Heller et al., 2014; Bhandari et al., 2015). Thus, in the context of the $A\sqrt{k_m}$ model, Patzek et al.'s (2014) model would require two to three times as much surface area as generated by the hydraulic fractures because the matrix permeability is almost an order of magnitude less than the assumed value. In fact, a lower bound estimate of the cumulative surface area represented by the shear fracture network from the five stages in the Barnett 1 data set is slightly more than the area of the hydraulic fractures themselves, resulting in more than twice as much total surface area in contact with the matrix.

In some ways, this simple argument addresses two fundamental questions about the field procedures that have proven to be successful in exploiting ultra-low permeability unconventional reservoirs. First, *why slick water?* Despite the fact that low-viscosity slick water is efficient in transporting proppant along a hydraulic fracture plane, it is needed to promote pressure leak-off from the hydraulic fractures to stimulate slip on preexisting fractures and faults in the volume of rock surrounding the hydraulic fractures. Creation of a permeable shear fracture network dramatically increases the contact area between the extremely low-permeability matrix and much more permeable fracture planes. Second, *why does the robustness of the microseismic cloud matter?* Whereas several authors have pointed to the importance of the shear fracture network (as indicated by the cloud of microseismic events), we attempt here to quantify this phenomenon in terms of a physical, if simple, flow model.

Another way to think about this is that the matrix permeability of unconventional reservoirs is so extremely low, and hydrocarbons can flow only a limited distance in a given amount of time. In other words, production rates are limited by the rate of diffusion from the matrix to the high-permeability fracture network (Walton and McLennan, 2013). In the context of linear flow, particle transport can be modeled by a 1D diffusive process, for which the characteristic diffusion time, τ is given by equation 6,

$$\tau = \frac{l^2}{\kappa} = \frac{(\phi B_f + B_r)\eta l^2}{k}, \quad (6)$$

where l is the characteristic diffusion distance, $\kappa \approx k\eta/(\phi B_f + B_r)$ is the hydraulic diffusivity, B_f and B_r are the fluid and rock compressibilities, respectively, ϕ is the rock porosity, and η is the fluid viscosity. Using mechanical properties of Barnett I cores at the relevant in situ stresses, the characteristic diffusion times can be constructed for various permeabilities using $B_f = 3 \times 10^{-8}$ Pa⁻¹, $B_r = 6 \times 10^{-11}$ Pa⁻¹, $\phi = 0.1$, and $\eta = 3.5 \times 10^{-5}$ Pa · s. The resulting relationship for natural gas and oil in linear and log space is shown in black and red, respectively,

in Figure 6. The three year characteristic diffusion distance for gas in a 100 nD reservoir is approximately 10 m. Fundamentally, this means that in three years, gas can flow only approximately 10 m from the pores in the matrix to a permeable fracture. The average perforation spacing in the Barnett I well is 40 m. Figure 6 suggests that if the hydraulic fracture spacing was 20 m, it would be possible to access the hydrocarbons between each hydraulic fracture effectively, even with a matrix permeability of 100 nD. However, one cannot reduce hydraulic spacing without the opening of one hydraulic fracture impeding the growth of nearby fractures (the so-called *stress shadow effect*, see, e.g., Kresse et al., 2013; Warpinski et al., 2013; Zoback and Kohli, 2019). Because of its higher viscosity, the situation is much worse for oil. For a matrix permeability of 100 nD, the diffusion distance is only approximately 2.5 m in three years.

Given the limited distance that gas or oil can flow in three years, it is important to stimulate slip on as many fractures and faults as possible in the volume of rock surrounding the hydraulic fractures. In a comprehensive set of 3D reservoir simulations of several unconventional plays in the United States, Sen et al. (2018) investigate optimal well spacing of wells, the spacing of perforation clusters, and the size of completions over different periods of production. This study is noteworthy in that rather than attempting to history match well production, they successfully matched stimulation treatment pressures, flowback rates, pressure build-up tests, and production. Especially relevant to this paper, their models required a zone of enhanced matrix permeability that is symmetrically distributed around hydraulic fractures to represent slip on many small faults that slipped in shear due to pressure leak-off from the hydraulic fractures.

Next, we consider relative gas production from the eight stages indicated by distributed temperature sensing (DTS) in the Barnett II study, which allows us to compare relative stage-by-stage gas production with the relative surface area created during each stage. The eight histograms in Figure 7 display the number of microearthquakes extrapolated from observed earthquakes down to magnitude -2.25 associated with each of the eight hydraulic fracturing stages in Barnett II as well as the cumulative area created, calculated in the manner described above. The left side of the figure shows the relative production data calculated from DTS data obtained at two different times during production (Roy et al., 2014). The total size of the stimulated fracture network associated with each stage varies dramatically, ranging from less than 100 m^2 in stages 1 and 8 to nearly $30,000 \text{ m}^2$ in stage 5. The total surface area created in all the stages was at least $76,000 \text{ m}^2$.

The stages with most production (4, 5, and 6) are also the stages in which the most surface area was created. Whereas very little surface area was created by shearing in several stages, there is still a small amount of production, perhaps associated with the area of the hydraulic fractures themselves, or aseismic slip. The duration of injection required to achieve a significant amount of permeable area varies from stage to stage. In stage 2, the limited amount of surface area created occurred after 140 min of pumping, whereas almost none occurred after that amount of time in stage 4. It should be noted that area is assigned to a specific stage if the microseismic event occurred during that stage, independent of the location of the event. Because the distribution of microseismic event locations varies with respect to the positions of individual stages, area created in one stage may contribute to production in an adjacent stage. For example,

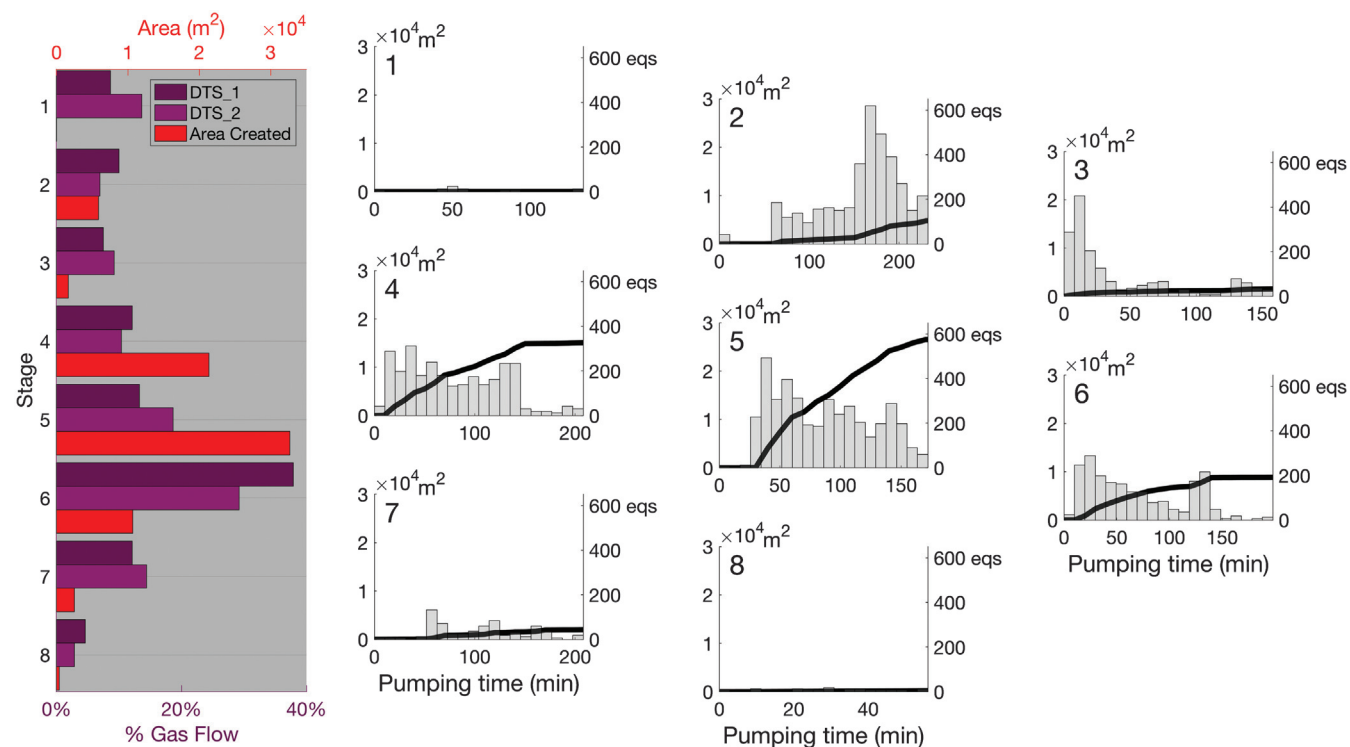


Figure 7. Each stage's contribution to total production, using distributed temperature sensing (from Roy et al. 2014), correlated with area created per stage (left). For each stage, the temporal distribution of microseismic event during injection is shown by the gray histogram. The cumulative area is indicated on the same axes by the black line.

microseismic events associated in time with stage 5 could be located in a place where they contribute more to production associated with stage 6. Indeed, the events associated with stages 5 and 6 overlap significantly (the right side of Figure 2). The point we make here is only that the robustness of the shear fracture network (as indicated by the microseismic cloud) is important (as pointed out in many previous studies).

Note that stage 2 has more microseismic events than stage 4 or 6, but the magnitudes of the events indicate that much less area was created and there was much less production. As Figure 7 does not consider the location of the events, the average magnitude of events during stage 2 must be smaller than that of stages 4 and 6.

In the context of Figure 6, by calculating the distribution of distances to permeable zones across the reservoir volume, we can estimate the drained portion of the volume associated with each stage as a function of time. Each stage that produced more than 5000 m² of area was associated with hundreds of earthquakes in the first hour of pumping, whereas stages 1, 7, and 8 saw little early microseismicity, and together they only produced a cumulative 1000 m² of area. To look at this another way, Figure 8 combines the concepts of area and diffusion time by characterizing the efficacy of each stage in terms of the distribution of diffusion times to the high-permeability fracture network in a volume with an average matrix permeability of 100 nD. The assumed reservoir volume is fixed for each stage. The dimensions are given by the well spacing, stage spacing, and thickness of the target formation, with the center

of the perforation cluster taken as the center of the volume. Following generation of the fracture network from microseismicity, a distribution of distances to the nearest stimulated fracture is calculated by randomly sampling from the space and calculating the distance to the nearest fracture. Converting from distance to mean diffusion time then provides insight into production over time using equation 6. This method excludes areas outside that surrounding each stage. For example, much of the area created by stage 2 was outside the target zone, resulting in only 22% of the adjacent reservoir volume being in the three year diffusion window. Note that the strong majority of the reservoir volume ultimately brought within three years of diffusion time to the permeable network is usually accessed in the first 90 min of pumping. Stage 7 is the only significant exception, where the amount of the reservoir volume accessed doubled between 90 and 180 min of pumping. In other words, this analysis suggests that far more fluid than necessary was pumped in seven of the eight stages.

CONCLUSION

The production decline rates in four unconventional gas and oil reservoirs in the continental United States indicate that linear flow dominates the economically crucial early years of production. The good fit of the production rates from the four reservoirs considered indicates that the rapid decrease in production rates is a natural consequence of depletion in these extremely low-permeability formations.

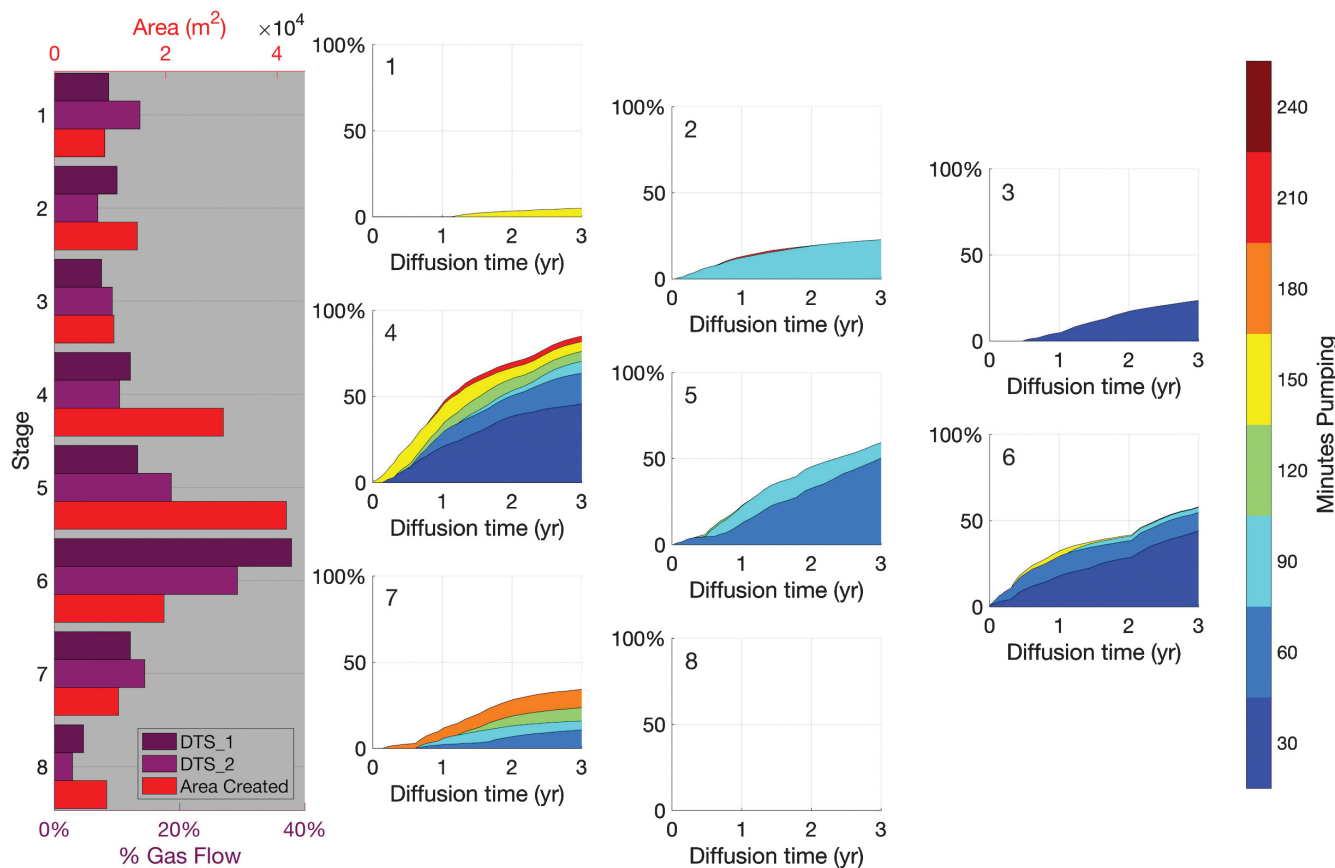


Figure 8. The percentage of the theoretical stimulated reservoir volume of each stage (on the y-axis) within a mean diffusion time (on the x-axis) is displayed as a function of time during stimulation (color contours), along with production by stage.

In this flow regime, production increases linearly with permeable surface area created through hydraulic fracturing and shearing of preexisting fractures and faults. The importance of the surface area created in the stimulated fracture network explains why slick water hydraulic fracturing is required in these extremely low-permeability reservoirs and why, as pointed out in several papers, there is a correlation between the robustness of the microseismic cloud created during slick water hydraulic fracturing and production. Accordingly, to maximize production, hydraulic fracturing stimulation should attempt to maximize area creation in a relatively well-distributed fracture network. We demonstrated that one can assess the evolution of cumulative surface area as injection proceeds. For the simple, first-order analysis presented here, neither precise event locations nor focal plane mechanisms are required.

DATA AND MATERIALS AVAILABILITY

Data associated with this research are confidential and cannot be released.

REFERENCES

- Al-Ismail, M. I., and M. D. Zoback, 2016, Effects of rock mineralogy and pore structure on extremely low stress-dependent matrix permeability of unconventional shale gas and shale oil samples: Philosophical Transactions of the Royal Society A: Mathematical, Physical and Engineering Sciences, **374**, 7–9, doi: [10.1098/rsta.2015.0428](https://doi.org/10.1098/rsta.2015.0428).
- Allmann, B. P., and P. M. Shearer, 2009, Global variations of stress drop for moderate to large earthquakes: Journal of Geophysical Research: Solid Earth, **114**, 1–22, doi: [10.1029/2008JB005821](https://doi.org/10.1029/2008JB005821).
- Arps, J. J., 1945, Analysis of decline curves: Transactions of the AIME, **160**, 228–247, doi: [10.2118/945228-G](https://doi.org/10.2118/945228-G).
- Bhandari, A. R., P. B. Flemings, P. J. Polito, M. B. Cronin, and S. L. Bryant, 2015, Anisotropy and stress dependence of permeability in the Barnett Shale: Transport in Porous Media, **108**, 393–411, doi: [10.1007/s11242-015-0482-0](https://doi.org/10.1007/s11242-015-0482-0).
- Cipolla, C., and J. Wallace, 2014, Stimulated reservoir volume: A misapplied concept?: Presented at the SPE Hydraulic Fracturing Technology Conference.
- Clerc, F., R. M. Harrington, Y. Liu, and Y. J. Gu, 2016, Stress drop estimates and hypocenter relocations of induced seismicity near Crooked Lake, Alberta: Geophysical Research Letters, **43**, 6942–6951, doi: [10.1002/2016GL069800](https://doi.org/10.1002/2016GL069800).
- Cocco, M., E. Tinti, and A. Cirella, 2016, On the scale dependence of earthquake stress drop: Journal of Seismology, **20**, 1151–1170, doi: [10.1007/s10950-016-9594-4](https://doi.org/10.1007/s10950-016-9594-4).
- Eaton, D. W., and S. Maghsoudi, 2015, 2b... or not 2b? Interpreting magnitude distributions from microseismic catalogs: First Break, **33**, 79–86.
- Farghal, N. S., and M. D. Zoback, 2015, Identification of slowly slipping faults in the Barnett Shale utilizing ant tracking; identification of slowly slipping faults in the Barnett Shale utilizing ant tracking: 85th Annual International Meeting, SEG, Expanded Abstracts, 4919–4923, doi: [10.1190/segam2015-5811224.1](https://doi.org/10.1190/segam2015-5811224.1).
- Gale, J. F. W., S. E. Laubach, J. E. Olson, P. Eichhuble, and A. Fall, 2014, Natural fractures in shale: A review and new observations: AAPG Bulletin, **98**, 2165–2216, doi: [10.1306/08121413151](https://doi.org/10.1306/08121413151).
- Goertz-Allmann, B. P., A. Goertz, and S. Wiemer, 2011, Stress drop variations of induced earthquakes at the Basel geothermal site: Geophysical Research Letters, **38**, 1–5, doi: [10.1029/2011GL047498](https://doi.org/10.1029/2011GL047498).
- Hakso, A., and M. Zoback, 2017, Utilizing multiplets as an independent assessment of relative microseismic location uncertainty: The Leading Edge, **36**, 829–836, doi: [10.1190/tle36100829.1](https://doi.org/10.1190/tle36100829.1).
- Heller, R., J. Vermulen, and M. Zoback, 2014, Experimental investigation of matrix permeability of gas shales: AAPG Bulletin, **98**, 975–995, doi: [10.1306/09231313023](https://doi.org/10.1306/09231313023).
- Huang, Y., G. C. Beroza, and W. L. Ellsworth, 2016, Stress drop estimates of potentially induced earthquakes in the Guy-Greenbrier sequence: Journal of Geophysical Research: Solid Earth, **121**, 6597–6607, doi: [10.1002/2016JB013067](https://doi.org/10.1002/2016JB013067).
- Imanishi, K., and W. L. Ellsworth, 2006, Source scaling relationships of microearthquakes at Parkfield, CA, determined using the SAFOD Pilot Hole seismic array, in R. Abercrombie, A. McGarr, and G. Di Toro, eds., *Earthquakes: Radiated energy and the physics of faulting*: American Geophysical Union, 81–90.
- Joshi, K., and W. J. Lee, 2013, Comparison of various deterministic forecasting techniques in shale gas reservoirs: Hydraulic Fracturing Technology Conference, SPE, doi: [10.2118/163870-MS](https://doi.org/10.2118/163870-MS).
- Kang, S. M., E. Fathi, R. J. Ambrose, I. Y. Akkutlu, and R. F. Sigal, 2011, Carbon dioxide storage capacity of organic-rich shales: SPE Journal, **16**, 842–855, doi: [10.2118/134583-PA](https://doi.org/10.2118/134583-PA).
- Katz, D. L., D. Cornell, R. Kobayashi, F. H. Poettmann, J. A. Vary, J. R. Ellenbass, and C. F. Weintraub, 1959, *Handbook of natural gas engineering: Natural gas engineering*: McGraw-Hill Book Company.
- Kohli, A. H., and M. D. Zoback, 2013, Frictional properties of shale reservoir rocks: Journal of Geophysical Research: Solid Earth, **118**, 5109–5125, doi: [10.1002/jgrb.50346](https://doi.org/10.1002/jgrb.50346).
- Kresse, O., X. Weng, H. Gu, and R. Wu, 2013, Numerical modeling of hydraulic fractures interaction in complex naturally fractured formations: Rock Mechanics and Rock Engineering, **46**, 555–568, doi: [10.1007/s00603-012-0359-2](https://doi.org/10.1007/s00603-012-0359-2).
- Kuang, W., M. Zoback, and J. Zhang, 2017, Estimating geomechanical parameters from microseismic plane focal mechanisms recorded during multistage hydraulic fracturing: Geophysics, **82**, no. 1, KS1–KS11, doi: [10.1190/geo2015-0691.1](https://doi.org/10.1190/geo2015-0691.1).
- Luffel, D. L., C. W. Hopkins, and P. D. Schettler, 1993, Matrix permeability measurement of gas productive shales: Annual Technical Conference and Exhibition, SPE, 261–271, doi: [10.2523/26633-MS](https://doi.org/10.2523/26633-MS).
- Maxwell, S. C., 2014, Microseismic imaging of hydraulic fracturing: SEG, Improved Engineering of Unconventional Shale Reservoirs.
- Maxwell, S. C., and C. L. Cipolla, 2011, What does microseismicity tell us about hydraulic fracturing?: Annual Technical Conference and Exhibition, SPE, doi: [10.2118/146932-MS](https://doi.org/10.2118/146932-MS).
- Maxwell, S. C., J. Shemeta, E. Campbell, and D. Quirk, 2008, Microseismic deformation rate monitoring: EAGE Passive Seismic Workshop — Exploration and Monitoring Applications, doi: [10.2118/116596-MS](https://doi.org/10.2118/116596-MS).
- Patzek, T., F. Male, and M. Marder, 2014, A simple model of gas production from hydrofractured horizontal wells in shales: AAPG Bulletin, **98**, 2507–2529, doi: [10.1306/03241412125](https://doi.org/10.1306/03241412125).
- Roy, B., B. Hart, A. Mironova, C. Zhou, and U. Zimmer, 2014, Integrated characterization of hydraulic fracture treatments in the Barnett Shale: The stocker geophysical experiment: Interpretation, **2**, no. 2, T111–T127, doi: [10.1190/INT-2013-0071.1](https://doi.org/10.1190/INT-2013-0071.1).
- Sen, V., K. S. Min, L. Ji, and R. Sullivan, 2018, Completions and well spacing optimization by dynamic SRV modeling for multi-stage hydraulic fracturing: Annual Technical Conference and Exhibition, SPE, doi: [10.2118/191571-MS](https://doi.org/10.2118/191571-MS).
- Stein, S., and M. Wysession, 2003, *An introduction to seismology, earthquakes, and earth structure*: John Wiley and Sons.
- Walton, I., and J. McLennan, 2013, The role of natural fractures in shale gas production, in R. Jeffrey, ed., *Effective and sustainable hydraulic fracturing*: IntechOpen.
- Warpinski, N. R., M. Mayerhofer, K. Agarwal, and J. Du, 2013, Hydraulic-fracture geomechanics and microseismic-source mechanisms: SPE Journal, **18**, 766–780, doi: [10.2118/158935-PA](https://doi.org/10.2118/158935-PA).
- Wu, W., J. S. Reece, Y. Gensterblum, and M. D. Zoback, 2017, Permeability evolution of slowly slipping faults in shale reservoirs: Geophysical Research Letters, **44**, 311–368, 375, doi: [10.1002/2017GL075506](https://doi.org/10.1002/2017GL075506).
- Ye, Z., M. Janis, A. Ghassemi, and S. Riley, 2017, Laboratory investigation of fluid flow and permeability evolution through shale fractures: Unconventional Resources Technology Conference, 24–26, doi: [10.15530/urtec-2017-2674846](https://doi.org/10.15530/urtec-2017-2674846).
- Zoback, M., and J.-E. Lund Snee, 2018, Predicted and observed shear on pre-existing faults during hydraulic fracture stimulation: 88th Annual International Meeting, SEG, Expanded Abstracts, 3588–3592, doi: [10.1190/segam2018-2991018.1](https://doi.org/10.1190/segam2018-2991018.1).
- Zoback, M. D., and A. H. Kohli, 2019, *Unconventional reservoir geomechanics*: Cambridge University Press.
- Zoback, M. D., A. Kohli, I. Das, and M. McClure, 2012, The importance of slow slip on faults during hydraulic fracturing stimulation of shale gas reservoirs: Americas Unconventional Resources Conference, SPE, doi: [10.2118/155476-MS](https://doi.org/10.2118/155476-MS).